Journal of Biomechanics 65 (2017) 203–211

Contents lists available at ScienceDirect

Journal of Biomechanics

journal homepage: www.elsevier.com/locate/jbiomech
www.JBiomech.com

Effect of integration time on the morphometric, densitometric and mechanical properties of the mouse tibia

S. Oliviero [a,b], Y. Lu [c], M. Viceconti [b,d], E. Dall'Ara [a,b,*]

[a] Department of Oncology and Metabolism, Mellanby Centre for Bone Research, University of Sheffield, UK
[b] Insigneo Institute for in silico Medicine, University of Sheffield, UK
[c] Department of Engineering Mechanics, Dalian University of Technology, China
[d] Department of Mechanical Engineering, University of Sheffield, UK

ARTICLE INFO

Article history:
Accepted 27 October 2017

Keywords:
Mouse tibia
micro-CT
Scanning
Morphometric
Bone mineral
Finite element

ABSTRACT

Micro-Computed Tomography (microCT) images are used to measure morphometric and densitometric properties of bone, and to develop finite element (FE) models to estimate mechanical properties. However, there are concerns about the invasiveness of microCT imaging due to the X-rays ionising radiation induced by the repeated scans on the same animal. Therefore, the best compromise between radiation dose and image quality should be chosen for each preclinical application. In this study, we investigated the effect of integration time (time the bone is exposed to radiation at each rotation step during microCT imaging) on measurements performed on the mouse tibia. Four tibiae were scanned at 10.4 μm voxel size using four different procedures, characterized by decreasing integration time (from 200 ms to 50 ms) and therefore decreasing nominal radiation dose (from 513 mGy to 128 mGy). From each image, trabecular and cortical morphometric parameters, spatial distribution of bone mineral content (BMC) in the whole tibia and FE-based estimations of stiffness and strength were obtained. A high-resolution scan (4.3 μm voxel size) was used to quantify measurement errors. Integration time had the largest effect on trabecular morphometric parameters (7–28%). Lower effects were observed on cortical parameters (1–3%), BMC (1–10%) distribution, and FE-based estimations of mechanical properties (1–3%). In conclusion, the effect of integration time on image-based measurements has been quantified. This data should be considered when defining the *in vivo* microCT scanning protocols in order to find the best compromise between nominal radiation exposure and accuracy in the estimation of bone parameters.

1. Introduction

Animal testing on small rodents has been used to investigate bone remodeling and to study the effect of bone interventions (Waarsing et al., 2004a). Micro-Computed Tomography (microCT) imaging is considered the gold standard for bone imaging and guidelines have been published regarding the image acquisition and analysis *ex vivo* or *in vivo* (Bouxsein et al., 2010). *In vivo* microCT imaging can be used to observe bone changes on the same bone over time (Bouxsein et al., 2010). This technique has been used in several studies to monitor the mouse tibia (Birkhold et al., 2014b, Brodt and Silva, 2010, Buie et al., 2008, Holguin et al., 2014) and caudal vertebra (Levchuk et al., 2014) longitudinally. Standard analyses of morphometric parameters in the tibia are performed in two volumes of interest (VOIs): a VOI below the proximal growth plate for trabecular bone analyses and a VOI at the midshaft for cortical bone analyses (Bouxsein et al., 2010). While it is known that local tissue mineral density (TMD) (Tassani et al., 2011) measurements at the voxel level are affected by microCT artifacts (Kazakia et al., 2008), this property can be measured over a larger VOI in order to account for potential changes in the tissue mineralization (Bouxsein et al., 2010). Lu and colleagues (Lu et al., 2017) recently proposed a method to analyze the spatio-temporal distribution of densitometric properties, e.g. bone mineral content (BMC), which is associated with a better repeatability than standard morphometric parameters (Lu et al., 2016) and provides comprehensive measurements over the whole bone. Furthermore, *in vivo* microCT images can be converted into finite element (FE) models (Patel et al., 2014, van Rietbergen et al., 1995) for non-invasive estimation of mechanical properties over time.

While longitudinal microCT imaging can be combined with other *in vivo* imaging modalities to study co-morbidities (Dall'Ara

* Corresponding author at: Insigneo Institute for in silico Medicine, University of Sheffield, Pam Liversidge building, Sheffield, S1 3JD, UK.
E-mail address: e.dallara@sheffield.ac.uk (E. Dall'Ara).

https://doi.org/10.1016/j.jbiomech.2017.10.026
0021-9290/

et al., 2016), there are concerns about its invasiveness due to the X-rays ionising radiation. Therefore, for the different applications, a compromise between the radiation dose and the image quality should be found. Image quality improves by decreasing the voxel size (Christiansen, 2016) and increasing the number of projections, the frame averaging and/or the integration time (Campbell and Sophocleous, 2014). However, in all cases the increase in the image signal-to-noise ratio is achieved by a longer scanning time, and consequently an increase in the induced radiation.

Previous studies have reported different results about the effect of radiation on bone. In some studies significant variations in morphometric parameters were observed in the mouse tibia, while no effect was found in other cases. Klinck and colleagues (Klinck et al., 2008) analyzed the effect of five scans (846 mGy) on the tibia in female mice of different strains (Table 1). In most groups, a significant reduction in trabecular bone volume fraction (BV/TV) was found. Additionally, significant increase in trabecular separation (Tb.Sp) or decrease in trabecular number (Tb.N) were observed in some of the analyzed groups of animals. Smaller effects were found on cortical parameters. Willie and colleagues (Willie et al., 2013) reported the effect of four scans (10.5 μm voxel size) in female C57BL/6J mice of different ages (Table 1). They observed a significant reduction in trabecular BV/TV and a significant increase in Tb.Sp in 10-week-old mice, while no effect was observed in 26 week old mice. On the other hand, Buie and colleagues (Buie et al., 2008) found no differences between animals scanned with low-radiation (6 scans at 188 mGy) or high-radiation (12 scans at 188 mGy) protocols, independently of the age (Table 1). Lastly, Laperre and colleagues (Laperre et al., 2011) found that three scans at 776 mGy induced a reduction in trabecular BV/TV and Tb.N in male C57Bl/6 mice (Table 1). Lower-radiation scanning protocols (434 mGy and 166 mGy) had no significant effect on trabecular or cortical parameters (Table 1). In all cases radiation had no significant effect on TMD, in both trabecular and cortical compartments (Table 1).

An effective strategy for obtaining low-radiation protocols could be to reduce the integration time (time the bone is exposed to radiation at each rotation step). It has been shown that variations in integration time do not affect the calibration curve for converting the X-ray attenuation coefficients into equivalent bone mineral density for different calibration phantoms (Nazarian et al., 2008). However, little is known about how a change in image quality due to the integration time would affect the microCT-based measurements performed on the mouse tibia.

The goal of this study was to investigate the effect of integration time on the measurement of mouse tibia morphometric, densitometric and mechanical properties, estimated with protocols that can be applied *in vivo*. Quantifying measurement errors is an essential step for selecting a suitable scanning protocol providing the best compromise between radiation dose and measurement accuracy.

2. Materials and methods

2.1. Sample preparation

Four tibiae (two right and two left) were explanted from 22-weeks-old C57BL/6J female mice used in a previous study (Lu et al., 2015). One of the mice underwent ovariectomy (OVX) and the other one was sham-operated (SHAM). Both surgeries were performed at week 14 of age. After carefully removing the soft tissues, the specimens were dehydrated in air at room temperature for 24 h and embedded in acrylic resin (Epofix, Struers, Denmark), which has a water equivalent attenuation coefficient. The specimens are referred to as OLT (OVX, left tibia), ORT (OVX, right tibia), SLT (SHAM, left tibia) and SRT (SHAM, right tibia).

The interested readers are welcome to contact the corresponding author who will share the data used in this study (https://doi.org/10.15131/shef.data.5562529.v1).

2.2. Scanning procedures and reconstructions

Each specimen was scanned using four different procedures (IT200, IT150, IT100 and IT50), suitable for *in vivo* application (VivaCT 80, Scanco Medical, Bruettisellen, Switzerland; 55 kVp, 145 μA, 10.4 μm voxel size, 32 mm field of view, 750 projections/180°, no frame averaging, 0.5 mm Al filter). Integration time was adapted for each protocol from 200 ms for IT200 to 50 ms for IT50. The IT200 protocol has been previously used for scanning the mouse tibia *in vivo* (Lu et al., 2016, Lu et al., 2017) and is associated with 513 mGy nominal radiation dose, which is comparable to that reported previously (Laperre et al., 2011) as acceptable for three *in vivo* scans. The other scanning protocols were associated to a reduced nominal radiation dose (384 mGy, 256 mGy and 128 mGy, respectively), as computed by using data from the manufacturer. All images were reconstructed using the software provided by the manufacturer (Scanco Medical AG) and applying a beam hardening correction based on a phantom of 1200 mg HA/cc density, which has been shown to improve the local tissue mineralization measurement (Kazakia et al. 2008).

Additionally, each specimen was scanned at higher resolution by using an *ex vivo* microCT (SkyScan 1172, Bruker, Belgium; 49 kV, 179 μA, 4.3 μm voxel size, 1180 ms exposure time, 180° rotation, 0.7° rotation step, frame averaging x2, 0.5 mm Al filter). These images were used as gold standard to quantify the measurements errors. Reconstruction was performed by using the software provided by the manufacturer (NRecon, Bruker; ring artifacts reduction factor 10, dynamic range 0–0.13) (Dudek et al., 2016, Mohanty et al., 2010). The same scanning and reconstruction protocols were used for imaging a four-insertion solid densitometric calibration phantom (MicroCT-HA, QRM, Germany).

The scanning and reconstruction procedures used for the two microCT systems were based on previously optimized protocols for *in vivo* (Lu et al., 2016, Lu et al., 2017) and *ex vivo* (Dudek et al., 2016, Mohanty et al., 2010) scans of the mouse tibia.

2.3. Image preprocessing

From each image three analyses were carried out (Fig. 1): standard morphometric analysis, spatial distribution of BMC and estimation of the mechanical properties with FE models.

One image was rotated in Amira (Amira 6.0.0, FEI Visualization Sciences Group, France) in order to approximately align its longitudinal axis to the *Z*-axis of a global reference system. Then, a rigid registration procedure was applied in order to align all images in the same reference system. Normalized Mutual Information was used as optimization criterion (Birkhold et al., 2014a). After alignment, images were resampled using Lanczos interpolator, which is associated to low interpolation errors (Meijering, 2000) and has been used in similar studies (Birkhold et al., 2014a). A Gaussian filter (kernel $3 \times 3 \times 3$, standard deviation 0.65) was applied to reduce the high frequency noise (Bouxsein et al., 2010).

2.4. Standard morphometric analysis

Morphometric analyses were performed using CTAn (Bruker, Belgium). For trabecular measurements, a reference slice was selected, identified as the slice where the medial and lateral sides

Table 1
Summary of the literature about the effect of radiation exposure on the mouse tibia. Groups: wild type (WT), ovariectomy (OVX), sham-operated (SHAM), *in vivo* cyclic compressive loading on the tibia (Loaded). Trabecular morphometric parameters: bone volume fraction (Tb.BV/TV), thickness (Tb.Th), separation (Tb.Sp), number (Tb.N), structure model index (SMI), degree of anisotropy (DA), connectivity density (Conn.D), tissue mineral density (Tb.TMD), bone mineral density (Tb.BMD). Cortical morphometric parameters: total cross-sectional area (Tt.Ar), cortical area (Ct.Ar), area fraction (Ct.Ar/Tt.Ar), thickness (Ct.Th), marrow area (Ma.Ar), tissue mineral density (Ct.TMD), polar moment of inertia (J), maximum moment of inertia (Imax), minimum moment of inertia (Imin).

Reference	Mouse strain	Age [weeks]	Gender	Group	Machine	Voxel size [μm]	Radiation dose [mGy]	Nr scans	Parameters investigated	Comparison with	Significant differences
Buie et al., (2008)	C3H/Hen C57BL/6J BALB/c	6	F	WT	VivaCT 40, Scanco Medical	19.0	188	12 (over 42 weeks)	Tb.BV.TV, Tb.Th, Tb.Sp, Tb.N, SMI, DA, Conn.D, Tb.TMD, Tb.BMD, Tt.Ar, Ct.Ar, Ct.Th, Ma.Ar, J	Group which underwent 6 scans at 188 mGy	No differences
Klinck et al., (2008)	C57BL/6J	12	F	WT	VivaCT 40, Scanco Medical	10.5	846	5 (every week)	Tb.BV/TV, Tb.Th, Tb.Sp, Tb.N, Ct.Ar, Ct.Th, Ma.Ar	Contralateral non-irradiated leg	Tb.N (−9.2%)
		12	F	OVX							Tb.BV/TV (−20.0%), Ma.Ar (−4.8%)
		12	F	SHAM							Tb.BV/TV (−14.0%), Ct.Ar (+5.7%), Ma.Ar (−3.6%)
	C3H/HeJ	12	F	WT							Tb.BV/TV (−8.0%), Tb.Sp (+9.6%)
		12	F	OVX							Tb.BV/TV (−19.4%), Tb.Sp (+14.4%), Tb.N (−11.3%), Ma.Ar (−3.4%)
		12	F	SHAM							Tb.BV/TV (−10.5%), Tb.Sp (+14.1%), Tb.N (−11.1%)
	BALB/cByJ	12	F	WT							Tb.BV/TV (−19.7%), Tb.Sp (+20.7%), Tb.N (−15.8%)
		12	F	OVX							Tb.BV/TV (−8.9%), Tb.Th (+8.9%), Tb.Sp (+18.3%), Tb.N (−14.2%), Ct.Th (+7.4%), Ma.Ar (−5.7%)
		12	F	SHAM							Tb.Th (+3.9%), Tb.N (−9.5%), Ct.Th (+4.7%)
Laperre et al., (2011)	C57Bl/6J	10	M	WT	SkyScan 1076, Bruker	9.0	776	3 (every 2 weeks)	Tb.BV/TV, Tb.Th, Tb.N, Tt.Ar, Ct.Ar, Ct.Th	Contralateral non-irradiated leg	Tb.BV/TV (−30%), Tb.N (−35%)
		4, 16	M	WT		9.0	434			Non-radiated group	No differences
		4, 16	M	WT		18.0	166			Non-radiated group	No differences
Willie et al., (2013)	C57BL/6J	10	F	WT	VivaCT 40, Scanco Medical	10.5	Not reported *(55 kVp, 145 uA, 600 ms integration time, no frame averaging)*	4 (every 5 days)	Tb.BV/TV, Tb.Th, Tb.Sp, Tb.N, Tb.TMD, Tt.Ar, Ct.Ar, Ct.Ar/Tt.Ar, Ct.Th, Ct.TMD, Imax, Imin	Single radiated group	Tb.BV/TV (−38%), Tb.Sp (+39%)
		10	F	Loaded							Tb.BV/TV (−20%), Tb.Sp (+29%)
		26	F	WT, Loaded							No differences

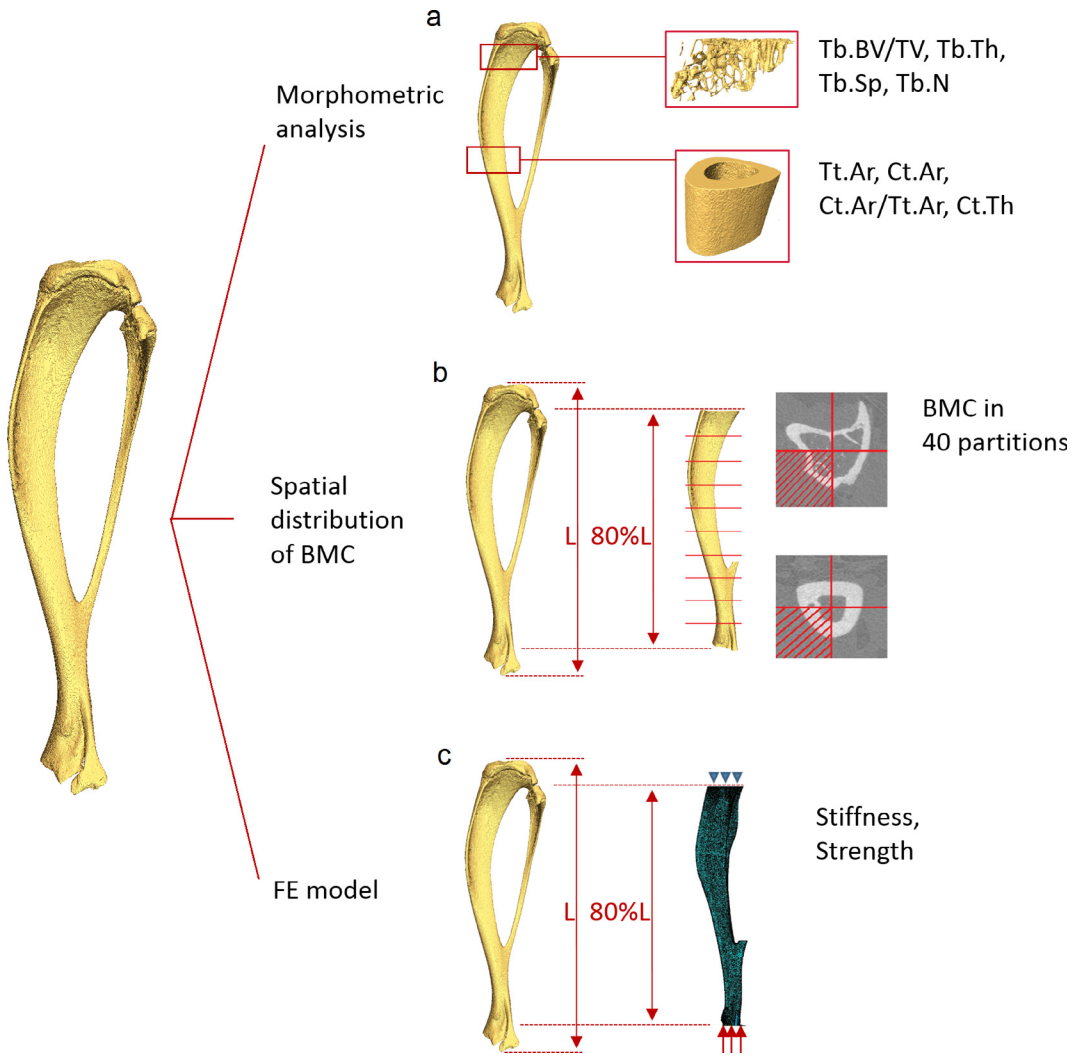

Fig. 1. Analyses performed on each microCT image of the mouse tibia. (a) Standard morphometric analysis of trabecular and cortical volumes of interest (VOIs) following the guidelines reported in (Bouxsein et al., 2010). Trabecular parameters: bone volume fraction (Tb.BV/TV), thickness (Tb.Th), separation (Tb.Sp) and number (Tb.N). Cortical parameters: total cross-sectional area (Tt.Ar), cortical area (Ct.Ar), area fraction (Ct.Ar/Tt.Ar), thickness (Ct.Th). (b) Spatial distribution of Bone Mineral Content (BMC). VOI consisted in the middle 80% of the tibia length (L) after removal of the fibula (Lu et al., 2016). The VOI was then divided in 10 equally spaced sections, which were further divided into four quadrants. (c) Finite Element (FE) models for estimation of stiffness and strength in uniaxial compression.

of the growth plate merged. An offset of 0.2 mm was used to identify the starting point of the VOI in the longitudinal direction and a VOI of 1 mm was selected (Lu et al., 2016). Trabecular bone was contoured by manually drawing 2D regions of interest every 5 slices. Segmentation was performed using a single level threshold, calculated for each image as the average of the grey levels corresponding to the bone and background peaks in the image histogram (Chen et al., 2017, Christiansen, 2016). A despeckling filter was applied to remove 3D white (bone) regions less than 10 voxels in volume, which are likely to be non-filtered noise. Trabecular bone volume fraction (Tb.BV/TV), thickness (Tb.Th), separation (Tb.Sp) and number (Tb.N) were computed (Bouxsein et al., 2010).

For cortical analysis, a VOI of 1 mm was selected, centered at the tibial midshaft. After segmentation, pores within the cortex were removed by applying a closing function (2D round kernel, 10 pixels radius). Total cross-sectional area (Tt.Ar), cortical bone area (Ct.Ar), cortical area fraction (Ct.Ar/Tt.Ar) and cortical thickness (Ct.Th) were computed (Bouxsein et al., 2010).

2.5. Spatial distribution of BMC

The co-registered grey-values (GV) images were converted into tissue mineral density (TMD) images by using the procedure suggested by the manufacturer of the *in vivo* scanner, which is based on weekly quality checks performed on a densitometric phantom with five insertions (800, 400, 200, 100 and 0 mg HA/cc). The GV of the reference high-resolution images (*ex vivo*) were converted into TMD scale by using the following linear regression equation (coefficient of determination $R^2 = 0.998$), obtained by scanning a calibration phantom (MicroCT-HA, QRM, Germany) with five insertions (1200, 800, 200, 50 and 0 mgHA/cc):

$$\text{TMD}\ [\text{mg HA/cc}] = 8.471 \times \text{GV} - 175.611 \quad (1)$$

BMC in each voxel was then calculated as its TMD multiplied by the volume of the voxel. The BMC was calculated in different regions of the tibia by applying a procedure similar to that reported by (Lu et al., 2016), which is briefly explained here. The VOI was defined by excluding the proximal and distal extremities (by 10%

of the total length), and the fibula (Fig.1b). The VOI was divided into ten longitudinal sections and each section was divided into four quadrants. Quadrants were defined by two perpendicular lines passing through the center of mass of each slice (Fig. 1b). Therefore, each tibia was divided into 40 partitions. For each partition, BMC was calculated as the sum of the BMC in each bony voxel.

2.6. Finite element models

Finite Element (FE) models were generated for the same VOI used for BMC analysis. Segmentation was performed using a single level threshold (average of the grey levels corresponding to the bone and background peaks in the image histogram). A connectivity filter was applied in order to remove unconnected voxels (connectivity rule = 6, bwlabeln function in Matlab). A Cartesian mesh was obtained by converting each bone voxel into an 8-noded hexahedral element (Chen et al., 2017, Patel et al., 2014) with isotropic linear elastic material properties (Young's Modulus = 14.8 GPa, Poisson's ratio = 0.3, (Vickerton et al., 2014, Webster et al., 2008)).

In order to evaluate the stiffness of the bone, uniaxial compression simulations were run in displacement control. The proximal side of the tibia was fully constrained, while a displacement of 1 mm was applied on each node of the distal surface along the longitudinal direction. The apparent stiffness was calculated as the sum of reaction forces at the proximal surface, divided by the applied displacement.

For strength estimation, uniaxial compression simulations were run in force control. The proximal nodes were fully constrained, while 1 N load was applied on the distal surface, equally distributed on each node. We assumed that tibia fails when 2% of the nodes reach a critical strain level (adapted from (Pistoia et al., 2002)), which was asymmetric for compression (−10,300 με) or tension (8000 με) (Bayraktar et al., 2004).

3. Results

3.1. Images and frequency plots

In Fig.2 examples of microCT cross-sections are reported, while in Fig.3 examples of image histograms (frequency plot) are shown for the *in vivo* (Fig.3a) and the *ex vivo* (Fig.3b) scanning procedures. When integration time was maximum (200 ms) the bone and background peaks were sharper, while with decreased integration time, higher variability was found in the grey values, indicating that the image was affected by higher noise.

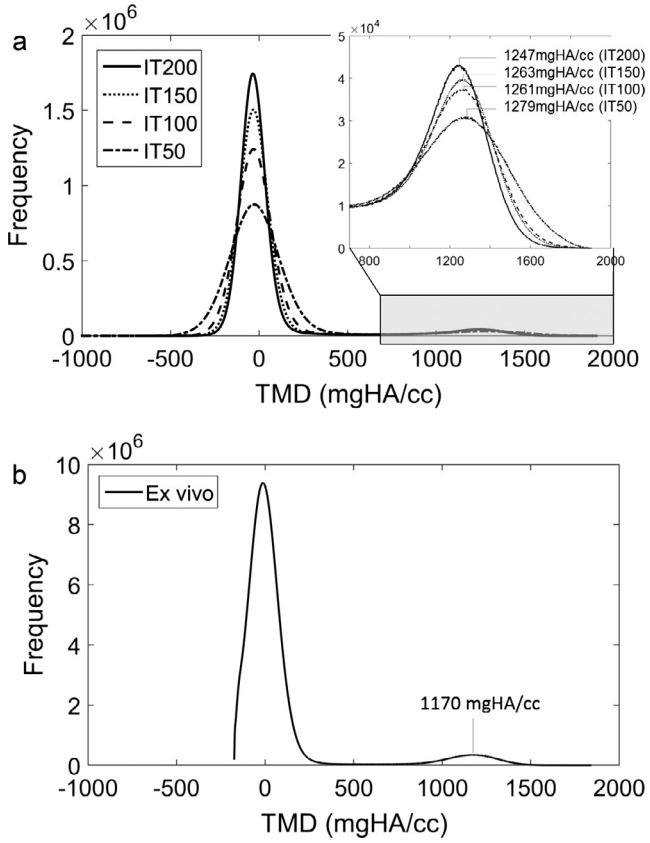

Fig. 3. Histograms (frequency plots) from microCT images obtained using the four *in vivo* (a) and the ex vivo (b) scanning procedures (OLT sample). IT200, IT150, IT100 and IT50 refer to scanning protocols with 200, 150, 100 and 50 ms integration time, respectively.

3.2. Morphometric analysis

The absolute percentage errors (median ± SD) for trabecular morphometric parameters measured with the *in vivo* scanning protocols compared to those obtained from high-resolution images are reported in Fig. 4a. For all parameters a converging trend was observed, meaning that the errors tend to stabilize with increasing integration time. However, errors tended to increase with integration time, while the opposite trend was expected. This was probably attributed to the presence of a systematic error, as discussed

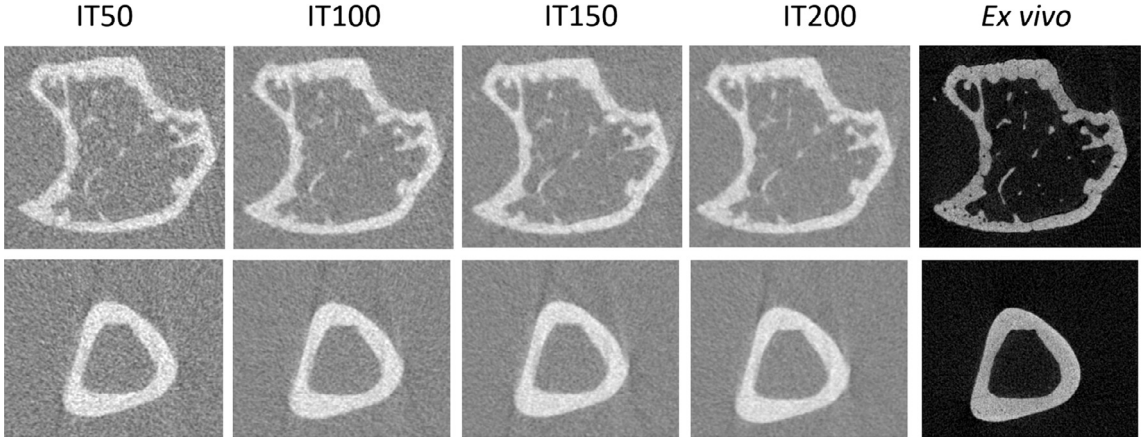

Fig. 2. MicroCT cross-sections of the trabecular (top row) and cortical (bottom row) regions of the tibia (SLT sample) scanned using the four *in vivo* (IT50 = 50 ms, IT100 = 100 ms, IT150 = 150 ms, IT200 = 200 ms integration time) and the ex vivo scanning procedures.

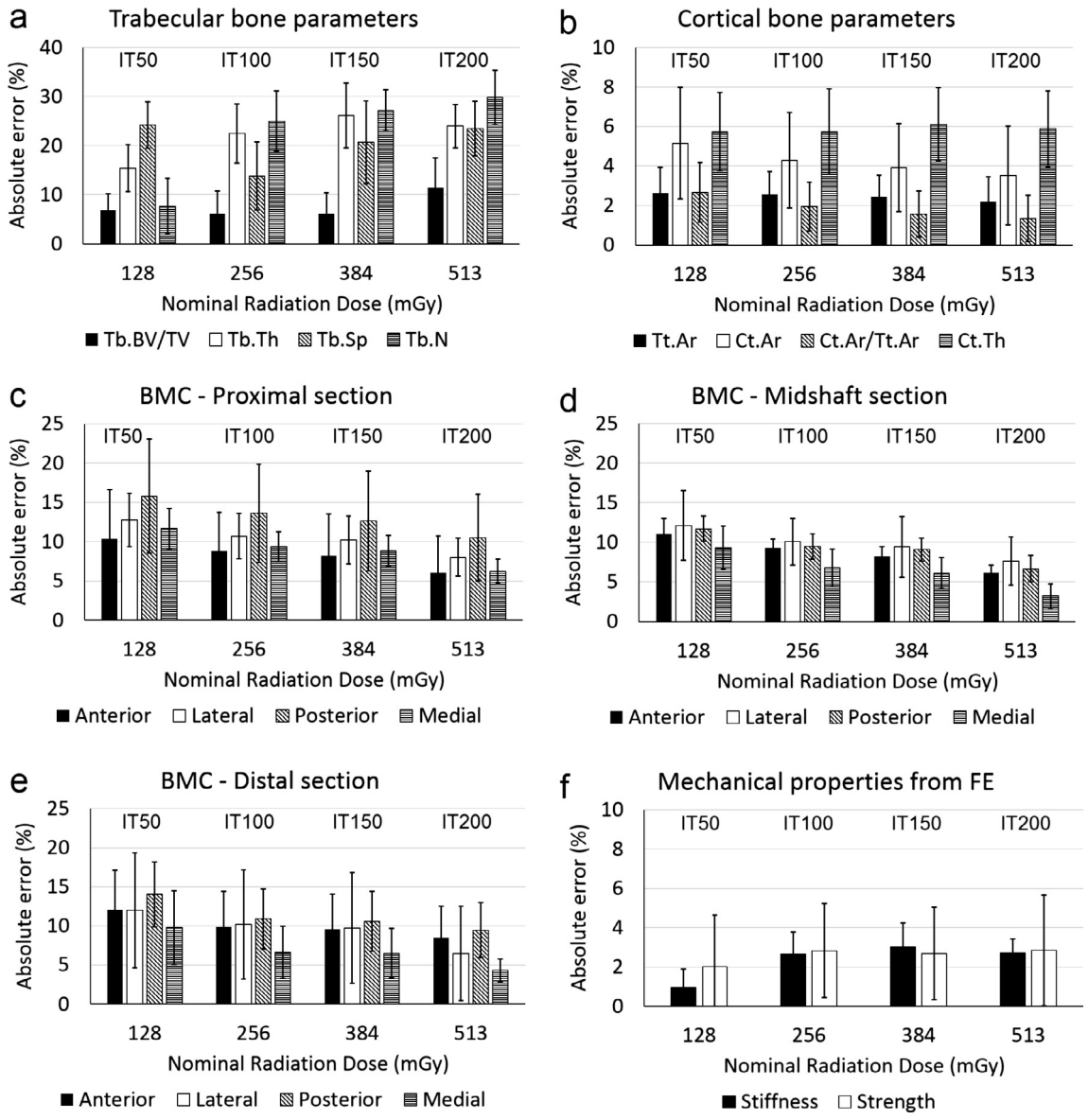

Fig. 4. Effect of scanning procedure on trabecular (a) and cortical (b) morphometric parameters, bone mineral content (BMC) in the proximal (c), medial (d) and distal (e) partitions, estimations of stiffness and strength from finite element (FE) models (f). Absolute errors are reported as median ± SD. IT200, IT150, IT100 and IT50 refer to scanning protocols with 200, 150, 100 and 50 ms integration time respectively, associated with a nominal radiation dose of 128, 256, 384 and 513 mGy respectively. Trabecular parameters: bone volume fraction (Tb.BV/TV), thickness (Tb.Th), separation (Tb.Sp) and number (Tb.N). Cortical parameters: total cross-sectional area (Tt.Ar), cortical area (Ct.Ar), area fraction (Ct.Ar/Tt.Ar), thickness (Ct.Th).

later. For Tb.BV/TV errors ranged from 2–11% for the IT50 scanning procedure, to 1–15% for IT200. For Tb.Th errors were 10–21% for IT50, 19–33% for IT100, 21–36% for IT150, and 22–32% for IT200. For Tb.Sp errors were 19–28% for IT50, 13–27% for IT100, 18–37% for IT150, and 19–31% for IT200. The greatest effect of integration time was found for Tb.N (from 1–13% for IT50 to 20–32% for IT200).

Errors associated to cortical parameters tended to decrease or be similar with increasing integration time (Fig. 4b). The largest effect was found for Ct.Ar (from 5–11% for IT50 to 3–8% for IT200), while minor effects were observed on Tt.Ar (from 2–5% for IT50 to 1–4% for IT200), Ct.Ar/Tt.Ar (from 2–6% for IT50 to 1–4% for IT200) and Ct.Th (4–9% for all procedures).

3.3. Spatial distribution of BMC

In Fig. 4c–e, absolute errors (median ± SD) for BMC measurements are reported for three out of ten longitudinal sections. For each section, the values associated to the four sectors are reported (anterior, lateral, posterior and medial). Partition 1 was the most proximal portion of the VOI, partition 5 was the middle one and partition 10 was the most distal portion of the VOI. Similar trends were found for all sub-regions. In all cases, errors decreased with increasing integration time. Errors were in the ranges of 1–28% for IT50, 1–24% for IT100, 1–24% for IT150, and 0–20% for IT200. The highest errors and variability were found in the proximal partitions (Fig. 4c), probably due to the presence of the trabecular region, while lower errors were found for the partitions located in the medial region (Fig. 4d).

3.4. Finite element models

FE models generated from high resolution images contained about 120 million elements and required about three hours CPU time for meshing and 270 h CPU time for each simulation (HPC

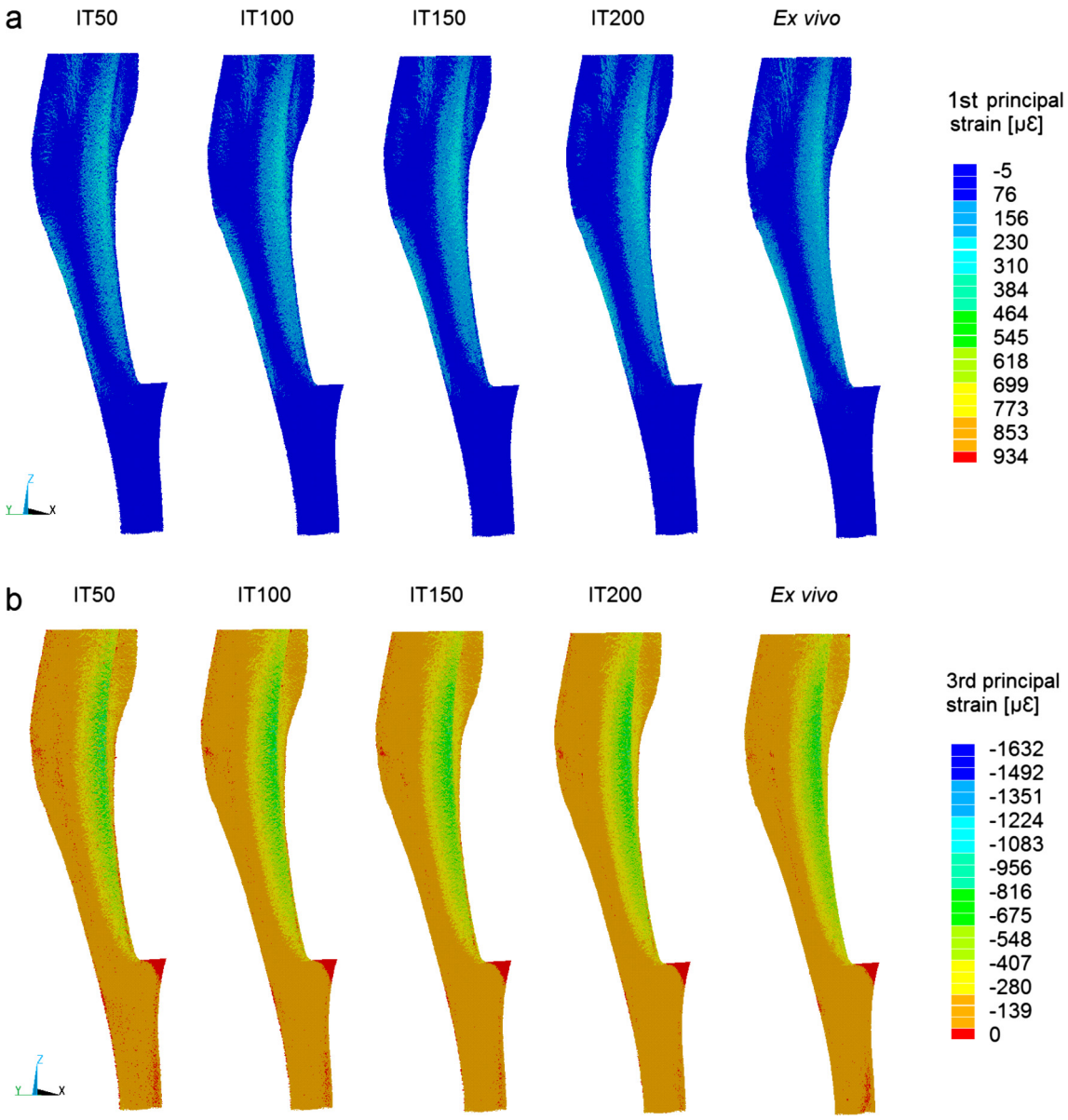

Fig. 5. Distribution of first (a) and third (b) principal strains over the tibia for the four *in vivo* scanning procedures (IT50, IT100, IT150 and IT200 correspond to 50, 100, 150 and 200 ms integration time, respectively) and the ex vivo scanning procedure (SRT sample).

Beagle, INSIGNEO, University of Sheffield; 64 cores, maximum memory = 738 GB). FE models developed for the other procedures contained approximately 10 million elements and required about 30 min CPU time for meshing and 23 h CPU time for each simulation (64 cores, maximum memory = 75 GB).

The effect of integration time on estimated mechanical properties was minor and errors were low for all procedures (0–4% for stiffness, 1–7% for strength, Fig. 4f). Comparable strain distributions were found for all scanning procedures (Fig. 5). In uniaxial compression, the maximum compressive strains were located at the curvature of the tibia (Fig. 5b).

4. Discussion

The effect of image quality, tuned by changing the integration time in microCT scanning procedure, was evaluated on morphometric, densitometric and mechanical measurements for the mouse tibia. The goal of the study was to quantify the measurements errors associated with each scanning procedure. The results showed a large dependency of the trabecular parameters on the integration time, weaker dependency for cortical areas and BMC distribution, and minor effect on cortical thickness and mechanical properties estimated by the FE models.

For trabecular morphometric parameters, the integration time led to large differences in measurements errors, up to 10% for Tb.BV/TV, 14% for Tb.Th, 16% for Tb.Sp and 28% for Tb.N. Errors showed a converging trend for increasing integration time, however errors tended to increase with integration time while the opposite trend was expected. This is probably due to the different partial volume effect in the *in vivo* (voxel size 10.4 μm, best achievable with our *in vivo* microCT) and *ex vivo* (voxel size 4.3 μm) scanning protocols. In a previous study, it has been shown that increasing the voxel size leads to overestimations in trabecular bone volume fraction and trabecular thickness (Christiansen, 2016). The segmentation method can also affect the measurements accuracy significantly (Christiansen, 2016). However, there is no consistent segmentation method among different studies

(Bouxsein et al., 2010) and threshold values from 420 mg HA/cc (Klinck et al., 2008) to 813 mg HA/cc (Birkhold et al., 2014a) have been reported. With our method (i.e. midpoint between the bone and background peaks in the histogram) threshold values of 499–568 mg HA/cc were obtained, which led to repeatable and user-independent segmentation among different samples and scanning procedures. By varying the threshold value in the range of those reported in literature, higher or comparable absolute errors were found (supplementary materials, Section 1).

Cortical parameters were characterized by smaller errors and smaller effect of integration time (maximum differences of 1–3%). As expected, lower errors for higher integration time were found for most cortical parameters, with the exception of Ct.Th, which seemed not to be affected. The weak dependency of the cortical parameters on integration time can be linked to the simplified structure to be analyzed compared to the complex trabecular structure, which has thinner features and larger bone surface.

Errors in BMC estimations showed similar trends, with errors decreasing with increasing integration time. Nevertheless, the influence of integration time was smaller (1–10%) compared to trabecular morphometric parameters. This is probably due to the fact that BMC measurements are less affected by the segmentation procedure and are more reproducible than morphometric measurements (Lu et al., 2016). Complementary data on the spatial distribution of TMD can be found in the supplementary materials (Section 2), showing that integration time led to differences of 1–7% in local TMD measurements.

Stiffness and strength estimated by the FE models were almost independent from integration time (differences of 1–3%). Since the overall mechanical properties of the tibia under uniaxial compression are mainly determined by the cortical bone (Supplementary material, Section 3), this result is consistent with the low effect of integration time on the cortical parameters. In fact, the maximum strains were localized at the curvature of the tibia, in the cortical compartment (Fig. 5). A similar finding was reported by Yang and colleagues (Yang et al., 2014), who found the maximum compressive and tensile strains in the trabecular bone to be 10% and 34% lower than those estimated at the midshaft, by simulating uniaxial compression of the whole tibio-fibular structure.

The main limitation of this study is the low sample size (four). Nevertheless, a comprehensive analysis has been performed for each of them, including the analysis of bone microstructure in the trabecular and cortical regions, the spatial distribution of bone mineral content and tissue mineral density in the whole tibia, and the mechanical properties estimated with specimen-specific FE models. Although the absolute errors for most properties were different among the specimens, their trends in function of the integration time were similar, suggesting that the reduction of this scanning parameter could be a good strategy for limiting the radiation dose. Possible improvements in the measurement of trabecular morphometric parameters could be achieved by applying more advanced segmentation techniques (Buie et al., 2007, Waarsing et al., 2004b). Finally, the FE models used in this study were based on a Cartesian mesh and on the assumption that bone is homogeneous, isotropic and linear elastic. While the goal of this study was to evaluate the effect of the IT on the mechanical properties estimated with the most common FE modelling approach, in the future the models could be improved by using a tetrahedral nonlinear mesh and accounting for local mineral heterogeneity and local material nonlinearities.

In conclusion, in this study we investigated the effect of decreasing the integration time for microCT scans of the mouse tibia. Our results quantify the measurement errors obtained using different scanning procedures and show that the cortical parameters and the FE model outputs are less sensitive to the chosen integration time. Therefore, in case these parameters have to be computed, shorter scans can be performed, reducing the potential effect of radiation dose, anesthesia and moving artifacts.

Acknowledgements

The authors acknowledge Dr Maya Boudiffa (skeletAL, http://skeletal.group.shef.ac.uk/) for her support with microCT imaging, Dr Yuan Chen for his assistance with FE modelling, Prof Ilaria Bellantuono and Prof Tim Skerry for the fruitful discussions. The study was funded by the UK National Centre for the Replacement, Refinement and Reduction of Animals in Research (NC3Rs, Grant number: NC/K000780/1) and by the Engineering and Physical Sciences Research Council (EPSRC, MultiSim project, Grant number: EP/K03877X/1).

Conflict of interest

None declared.

Appendix A. Supplementary material

Supplementary data associated with this article can be found, in the online version, at https://doi.org/10.1016/j.jbiomech.2017.10.026.

References

Bayraktar, H.H., Morgan, E.F., Niebur, G.L., Morris, G.E., Wong, E.K., Keaveny, T.M., 2004. Comparison of the elastic and yield properties of human femoral trabecular and cortical bone tissue. J. Biomech. 37, 27–35.
Birkhold, A.I., Razi, H., Duda, G.N., Weinkamer, R., Checa, S., Willie, B.M., 2014a. Mineralizing surface is the main target of mechanical stimulation independent of age: 3D dynamic in vivo morphometry. Bone 66, 15–25.
Birkhold, A.I., Razi, H., Duda, G.N., Weinkamer, R., Checa, S., Willie, B.M., 2014b. The influence of age on adaptive bone formation and bone resorption. Biomaterials 35, 9290–9301.
Bouxsein, M.L., Boyd, S.K., Christiansen, B.A., Guldberg, R.E., Jepsen, K.J., Müller, R., 2010. Guidelines for assessment of bone microstructure in rodents using micro–computed tomography. J. Bone Miner. Res. 25, 1468–1486.
Brodt, M.D., Silva, M.J., 2010. Aged mice have enhanced endocortical response and normal periosteal response compared with young-adult mice following 1 week of axial tibial compression. J. Bone Miner. Res. 25, 2006–2015.
Buie, H.R., Campbell, G.M., Klinck, R.J., Macneil, J.A., Boyd, S.K., 2007. Automatic segmentation of cortical and trabecular compartments based on a dual threshold technique for in vivo micro-CT bone analysis. Bone 41, 505–515.
Buie, H.R., Moore, C.P., Boyd, S.K., 2008. Postpubertal architectural developmental patterns differ between the L3 vertebra and proximal tibia in three inbred strains of mice. J. Bone Miner. Res. 23, 2048–2059.
Campbell, G.M., Sophocleous, A., 2014. Quantitative analysis of bone and soft tissue by micro-computed tomography: applications to ex vivo and in vivo studies. BoneKEy Rep. 3.
Chen, Y., Dall'ara, E., Sales, E., Manda, K., Wallace, R., Pankaj, P., Viceconti, M., 2017. Micro-CT based finite element models of cancellous bone predict accurately displacement once the boundary condition is well replicated: a validation study. J. Mech. Behav. Biomed. Mater. 65, 644–651.
Christiansen, B.A., 2016. Effect of micro-computed tomography voxel size and segmentation method on trabecular bone microstructure measures in mice. Bone Rep. 5, 136–140.
Dall'ara, E., Boudiffa, M., Taylor, C., Schug, D., Fiegle, E., Kennerley, A.J., Damianou, C., Tozer, G.M., Kiessling, F., Müller, R., 2016. Longitudinal imaging of the ageing mouse. Mech. Ageing Dev. 160, 93–116.
Dudek, M., Gossan, N., Yang, N., Im, H.-J., Ruckshanthi, J.P.D., Yoshitane, H., Li, X., Jin, D., Wang, P., Boudiffa, M., Bellantuono, I., Fukada, Y., Boot-Handford, R.P., Meng, Q.-J., 2016. The chondrocyte clock gene Bmal1 controls cartilage homeostasis and integrity. J. Clin. Investig. 126, 365–376.
Holguin, N., Brodt, M.D., Sanchez, M.E., Silva, M.J., 2014. Aging diminishes lamellar and woven bone formation induced by tibial compression in adult C57BL/6. Bone 65, 83–91.
Kazakia, G.J., Burghardt, A.J., Cheung, S., Majumdar, S., 2008. Assessment of bone tissue mineralization by conventional x-ray microcomputed tomography: comparison with synchrotron radiation microcomputed tomography and ash measurements. Med. Phys. 35, 3170–3179.
Klinck, R.J., Campbell, G.M., Boyd, S.K., 2008. Radiation effects on bone architecture in mice and rats resulting from in vivo micro-computed tomography scanning. Med. Eng. Phys. 30, 888–895.

Laperre, K., Depypere, M., van Gastel, N., Torrekens, S., Moermans, K., Bogaerts, R., Maes, F., Carmeliet, G., 2011. Development of micro-CT protocols for in vivo follow-up of mouse bone architecture without major radiation side effects. Bone 49, 613–622.

Levchuk, A., Zwahlen, A., Weigt, C., Lambers, F.M., Badilatti, S.D., Schulte, F.A., Kuhn, G., Müller, R., 2014. The Clinical Biomechanics Award 2012 – presented by the European Society of Biomechanics: large scale simulations of trabecular bone adaptation to loading and treatment. Clin. Biomech. 29, 355–362.

Lu, Y., Boudiffa, M., Dall, Ara, E., Bellantuono, I., Viceconti, M., 2015. Evaluation of in-vivo measurement errors associated with micro-computed tomography scans by means of the bone surface distance approach. Med. Eng. Phys. 37, 1091–1097.

Lu, Y., Boudiffa, M., Dall'Ara, E., Bellantuono, I., Viceconti, M., 2016. Development of a protocol to quantify local bone adaptation over space and time: Quantification of reproducibility. J. Biomech., 2095–2099

Lu, Y., Boudiffa, M., Dall'ara, E., Liu, Y., Bellantuono, I., Viceconti, M., 2017. Longitudinal effects of Parathyroid Hormone treatment on morphological, densitometric and mechanical properties of mouse tibia. J. Mech. Behav. Biomed. Mater. 75, 244–251.

Meijering, E.H.W., 2000. Spline interpolation in medical imaging: comparison with other convolution-based approaches. In: Signal Processing Conference, 2000 10th European, 4–8 Sept. 2000, pp. 1–8.

Mohanty, S.T., Kottam, L., Gambardella, A., Nicklin, M.J., Coulton, L., Hughes, D., Wilson, A.G., Croucher, P.I., Bellantuono, I., 2010. Alterations in the self-renewal and differentiation ability of bone marrow mesenchymal stem cells in a mouse model of rheumatoid arthritis. Arthrit. Res. Ther. 12. R149–R149.

Nazarian, A., Snyder, B.D., Zurakowski, D., Müller, R., 2008. Quantitative micro-computed tomography: a non-invasive method to assess equivalent bone mineral density. Bone 43, 302–311.

Patel, T.K., Brodt, M.D., Silva, M.J., 2014. Experimental and finite element analysis of strains induced by axial tibial compression in young-adult and old female C57Bl/6 mice. J. Biomech. 47, 451–457.

Pistoia, W., van Rietbergen, B., Lochmüller, E.M., Lill, C.A., Eckstein, F., Rüegsegger, P., 2002. Estimation of distal radius failure load with micro-finite element analysis models based on three-dimensional peripheral quantitative computed tomography images. Bone 30, 842–848.

Tassani, S., Öhman, C., Baruffaldi, F., Baleani, M., Viceconti, M., 2011. Volume to density relation in adult human bone tissue. J. Biomech. 44, 103–108.

van Rietbergen, B., Weinans, H., Huiskes, R., Odgaard, A., 1995. A new method to determine trabecular bone elastic properties and loading using micromechanical finite-element models. J. Biomech. 28, 69–81.

Vickerton, P., Jarvis, J.C., Gallagher, J.A., Akhtar, R., Sutherland, H., Jeffery, N., 2014. Morphological and histological adaptation of muscle and bone to loading induced by repetitive activation of muscle. Proc. Roy. Soc. Lond. B: Biol. Sci. 281, 20140786. 20140786-20140786.

Waarsing, J.H., Day, J.S., van der Linden, J.C., Ederveen, A.G., Spanjers, C., de Clerck, N., Sasov, A., Verhaar, J.A.N., Weinans, H., 2004a. Detecting and tracking local changes in the tibiae of individual rats: a novel method to analyse longitudinal in vivo micro-CT data. Bone 34, 163–169.

Waarsing, J.H., Day, J.S., Weinans, H., 2004b. An Improved Segmentation Method for In Vivo μCT Imaging. J. Bone Miner. Res. 19, 1640–1650.

Webster, D.J., Morley, P.L., van Lenthe, G.H., Müller, R., 2008. A novel in vivo mouse model for mechanically stimulated bone adaptation – a combined experimental and computational validation study. Comput. Methods Biomech. Biomed. Eng. 11, 435–441.

Willie, B.M., Birkhold, A.I., Razi, H., Thiele, T., Aido, M., Kruck, B., Schill, A., Checa, S., Main, R.P., Duda, G.N., 2013. Diminished response to in vivo mechanical loading in trabecular and not cortical bone in adulthood of female C57Bl/6 mice coincides with a reduction in deformation to load. Bone 55, 335–346.

Yang, H., Butz, K.D., Duffy, D., Niebur, G.L., Nauman, E.A., Main, R.P., 2014. Characterization of cancellous and cortical bone strain in the in vivo mouse tibial loading model using microCT-based finite element analysis. Bone 66, 131–139.